



On the role of turbulence and compositional fluctuations in rapid compression machines: Autoignition of syngas mixtures

Matthias Ihme

Department of Aerospace Engineering, University of Michigan, Ann Arbor, MI 48109, United States

ARTICLE INFO

Article history:

Received 15 March 2011

Received in revised form 10 June 2011

Accepted 26 November 2011

Available online 24 January 2012

Keywords:

Rapid compression machine

Turbulence

Syngas

Autoignition

Integrated combined-cycle

Rapid distortion theory

ABSTRACT

With the increasing interest in utilizing syngas in gas turbine applications, the characterization of H_2/CO combustion and reaction chemistry under high-pressure and moderate-temperature operating conditions has been the focus of recent investigations. Different chemical-kinetics and hydrodynamic processes have been identified as being responsible for the discrepancies between experimental measurements and kinetic predictions of syngas ignition delay times. This contribution complements previous studies, and provides improved understanding about the role of turbulence and fluctuations in temperature and mixture composition on the syngas combustion process in rapid compression machines (RCMs). To this end, a self-contained model is developed that describes the ignition and combustion process by considering the interaction between turbulence, detailed reaction chemistry, and wall heat loss effects. Different mechanisms can be identified as being responsible for the generation of inhomogeneities in flow-field, temperature, and mixture composition, including turbulence-generation during the filling process, corner vortices, wall-generated turbulence, and mixing between fluid in the core region and the boundary layer. In the present model, these contributions are parametrically represented in terms of initial turbulence levels, and the mean-strain amplification of these perturbations during the compression phase is described using rapid distortion theory. The model is applied to different syngas mixtures and operating conditions, including pressures up to 20 atm and temperatures between 600 and 1300 K. Parametric studies show that the model captures experimentally observed trends of reduced ignition delay and prolonged reaction progress during the ignition phase. A Damköhler criterion is proposed in order to characterize the sensitivity of the induction chemistry to turbulence fluctuations. Results suggest that syngas mixtures with Damköhler numbers below 50 exhibit increasing sensitivity to turbulence and mixture fluctuations. This parametric study indicates that the turbulence/chemistry interaction can play an equally important role in affecting the syngas ignition chemistry, and requires consideration in addition to chemical-kinetics and hydrodynamic processes previously identified as leading mechanisms for the observed discrepancy in syngas ignition.

© 2011 The Combustion Institute. Published by Elsevier Inc. All rights reserved.

1. Introduction

Accompanied with the rapid economic growth in the developing nations of Asia is an increasing energy demand, which, according to the International Energy Outlook 2009 [1], is predicted to exceed the US energy consumption by more than 65% by 2030. In the presence of finite oil and gas reserves and growing environmental concerns, the utilization of reformed fuels provides an attractive alternative for accommodating the increasing energy demand. Among these reformed fuels, that can be derived from coal, biomass, organic waste, and other opportunity fuels, syngas is particularly attractive for power generation applications. In coal-based integrated gasification combined cycle (IGCC) gas turbines, syngas, containing hydrogen (H_2) and carbon monoxide (CO) as

primary fuel components, is generated through a coal gasification process [2]. After sulfur oxides, particulates and other pollutants are removed, the syngas is combusted in a gas turbine cycle, and excess heat is converted in a subsequent steam turbine cycle.

Despite enormous opportunities in improving combustion efficiency and reducing pollutant emissions, syngas combustion introduces significant technological and scientific challenges. These issues mainly arise from process-related variations in the syngas composition, high hydrogen concentrations, and overall lean operating conditions. In addition, IGCC gas turbines are operated under high pressure (up to 30 bar) and intermediate temperature ($T < 1000$ K) conditions, and the syngas combustion under these conditions is currently only insufficiently understood.

The renewed interest in syngas combustion led to numerous experimental studies in order to obtain improved understanding about the combustion-physical properties and reaction chemistry

E-mail address: mihme@umich.edu

Nomenclature*Upper-case roman letters*

<i>A</i>	RCM cross-sectional area
<i>C</i>	progress variable
<i>R</i>	gas constant
<i>T</i>	temperature
<i>W</i>	Wiener process, molecular weight
<i>Y</i>	species mass fraction vector
<i>Z</i>	mixture fraction

Lower-case roman letters

<i>c</i>	friction coefficient
<i>d</i>	diameter
<i>e</i>	unit wave number vector
<i>k</i>	turbulent kinetic energy
<i>l</i>	length
<i>m</i>	mass of the piston
<i>p</i>	pressure
<i>r</i>	radius
<i>t</i>	time
<i>u</i>	velocity vector
<i>x</i>	spatial location
<i>x</i>	coordinate vector

Upper-case greek letters

Θ	normalized temperature
----------	------------------------

Lower-case greek letters

α	strain rate
β	mixture stratification
γ	ratio of specific heats
δ	displacement thickness
ε	dissipation rate
κ, \varkappa	wave-number vector
λ	thermal conductivity

ν	kinematic viscosity
ξ	compression ratio
ρ	density
$\underline{\sigma}$	viscous stress tensor
τ	time scale
ν	species diffusivity
ϕ	equivalence ratio
ψ	generic thermochemical quantity
$\dot{\omega}$	source term

Superscripts

*	dimensional quantity
---	----------------------

Subscripts

0	end of compression phase
1	quantity related to driven section
2	quantity related to driver section
<i>p</i>	piston
<i>s</i>	initial state at beginning of compression phase
\downarrow	wall-heat-transfer-related quantity

Symbols and abbreviations

\mathcal{D}_t	substantial derivative
\mathcal{T}	Turbulence intensity, scalar fluctuation level
∂_ζ	partial derivative with respect to ζ
$\langle \psi \rangle$	volume-averaged quantity
$\overline{\psi}$	ensemble-averaged quantity
$\hat{\psi}$	Fourier mode
$\dot{\psi}$	temporal derivative
Da	Damköhler number
Ec	Eckert number
Le	Lewis number
Re	Reynolds number
Sc	Schmidt number

of syngas oxidation under gas-turbine-relevant operating conditions. These experiments are typically conducted in shock tubes (STs), flow reactors (FRs), and rapid compression machines (RCMs), and Refs. [3–6] provide comprehensive overviews about experimental investigations and measurements for ignition delay time, flame speed, and other combustion-physical properties.

Interestingly, comparisons of ignition delay times between measurements and computations exhibit significant discrepancies [6] that increase with decreasing initial temperature of the syngas/air mixture. To reconcile these discrepancies, different explanations have been proposed, including incomplete reaction mechanisms and uncertainties in rate constants, effects of gas impurities and surface-catalytic processes, wall-heat transfer and large-scale mixing, and drifts in operating conditions. Although some of these mechanisms are particular to specific facilities [7,8], the disparity of measurements among different facilities would suggest that such secondary processes might also be present at different levels in other facilities, and their potential contributions require careful characterization.

Over recent years, computational and experimental studies have been conducted to characterize the flow field structure and wall heat transfer in RCMs [9–14]. Intrusive and non-intrusive measurements of temperature and species have been performed to demonstrate the existence of a so-called adiabatic core region. In this adiabatic core region the gas mixture is not directly affected by heat losses and boundary layer effects. The mixture contained in this volume is isentropically compressed, and the combustion of

the nominally uniform composition can be approximated as a homogeneous reactor system. In this context it is noted that the existence of this adiabatic core region is fundamental in order to relate rapid compression experiments to zero-dimensional homogeneous ignition studies. Although this volumetric ignition scenario is the prevailing combustion mode in RCMs, deflagrative ignition modes have also been observed experimentally [5,14,15]. These front-like ignition modes have been associated with a gradual increase in the pressure trace [15]. Investigations by Elsworth et al. [15] and others suggest that these non-uniform ignition processes are initiated at particles that are present in the test gas mixture. They also concluded that deflagration modes become more relevant in hydrogen-containing mixtures, which was attributed to the enhanced sensitivity of these mixtures to impurities.

While experimental investigations mainly focused on the large-scale fluid motion and wall heat transfer effects, the role of turbulence and fluctuations in composition and temperature on the ignition and combustion in RCMs has so far not been appreciated. The objective of this contribution is to address this aspect. To this end, a model is developed that enables the characterization of turbulence fluctuations and variations in mixture composition and temperature during the compression and ignition of the gas mixture.

The potential importance of turbulence in RCMs can be assessed from the Reynolds number Re , which can be estimated as:

$$Re = \frac{l_1^*}{\tau^*} \frac{d^*}{\nu^*}, \quad (1)$$

where the ratio l_1^*/τ^* is the characteristic speed of the piston, l_1^* is the length of the RCM driven section, τ^* is the compression time, d^* is the diameter of the test section, and ν^* is the kinematic viscosity of the gas mixture at reference condition. Typical Reynolds numbers for RCMs are in the range $Re \approx \mathcal{O}(10^4 - 10^5)$, suggesting that the compression and subsequent ignition is not unaffected by turbulence. This argument is supported by recent investigations by Guibert et al. [14], in which PIV measurements in a RCM-facility were performed. These measurements showed that mean flow fluctuations above 5 m/s can be obtained at the end of the RCM compression phase. This magnitude is in qualitative agreement with turbulence measurements in idealized internal combustion engines [16].

The following sources of turbulence can be identified in RCMs:

- *Filling process*: The filling process of the driven section with the fresh test gas mixture is accompanied by the generation of small-scale turbulence fluctuations that are approximately homogeneously distributed in the entire test section. If the compression phase is initiated directly after the filling process, providing insufficient time for the complete decay, the initially introduced turbulence is amplified during the compression.
- *Corner vortices*: During the compression phase, the piston motion generates corner vortices and large vortical structures. The roll-up of these structures induces flow field perturbations and the entrainment of cold fluid into the core region [10,17]. Although these corner vortices can be reduced by appropriate piston-crown design [10,12], their contributions cannot be entirely eliminated.
- *Boundary layer-generated turbulence*: During the compression phase, the piston motion induces a mean flow, which leads to the formation of a boundary layer. At sufficiently high Reynolds numbers, the boundary layer transitions, which is associated with the generation of turbulence. This wall-generated turbulence is subsequently transported into the core region, where it will be further amplified through the mean strain interaction.
- *Turbulence production by compressive strain*: During the compression phase, the rapid piston motion induces a time-dependent strain rate, leading to enhanced turbulence production. This nonequilibrium process is dependent on the strain-rate profile, and is a main mechanism for the turbulence amplification at the end of the compression phase.

Although the relative contributions of these mechanisms have so far not been experimentally quantified and are most-likely dependent on facility design and operating conditions, theoretical investigations suggest that the mean-strain amplification is a main process for the turbulence-generation in piston compression machines [18–20].

In order to quantify the turbulence at the end of the RCM-compression phase, rapid distortion theory is utilized to model the turbulence amplification by the piston-induced mean-strain. Sources of turbulence that arise from the filling process, boundary-layer, and vortical roll-up are hereby considered as feeding mechanisms to this mean-strain amplification, and are in the following parametrically represented in terms of an initial turbulence level, which is denoted by \mathcal{T}_u .

Following the compression phase, the ignition of the test gas mixture is modeled by considering the distribution of thermal and mixture inhomogeneities, which interact among each other through turbulent mixing and diffusion. To this end, a Lagrangian Fokker–Planck (LFP) model is derived, and closure is obtained using a k - ε formulation and an IEM (“interaction by exchange with the mean”) micromixing model. The particular advantage of this model is that this LFP formulation reduces to the well-known

homogeneous reactor model in the absence of turbulence and mixture inhomogeneities.

The remainder of this paper is organized as follows. The details on the mathematical model are discussed in the next section. The experimental configuration and model parameters are summarized in Section 3, and results are presented in Section 4. Further extensions of the model and potential implications of the results with respect to multidimensional RCM simulations and HCCI-applications are discussed in Section 5, and the paper finishes with conclusions.

2. Mathematical model

In the following, a mathematical model is developed to describe the compression and subsequent combustion process in a rapid compression machine. This model development is guided by the interest in developing a low-order model that enables the identification of important process parameters and their effects on the ignition and combustion process in RCM-facilities. To this end, the RCM is modeled as a one-dimensional system and geometric variations due to contractions in the driven section are not considered. Such converging sections are utilized by different groups [14,21] to connect the driven and the test-gas regions. While such contractions are beneficial in preventing the boundary layer from entering the test-gas section, they locally enhance the strain and promote flow separation.

The schematic of the RCM is illustrated in Fig. 1, consisting of a driver section and a driven section; both sections are separated by a freely moving piston with mass m^* . A coordinate system x_1^* is introduced, and the location of the piston with respect to the coordinate origin is denoted by x_p^* . Conditions in the driven and the driver sections are denoted by subscripts “1” and “2”, respectively, and all dimensional quantities are indicated by an asterisk.

To describe the kinematics of the RCM during the compression phase, the following reference quantities are identified:

$$\text{Length scale : } l_1^* = x_p^*(t^* = 0),$$

$$\text{Time scale : } \tau^* = \sqrt{\frac{m^* l_1^*}{\Delta p^* A^*}},$$

$$\text{Pressure difference : } \Delta p^* = p_2^*(t^* = 0) - p_1^*(t^* = 0),$$

where p^* is the pressure and A^* is the constant piston area. With these reference properties, the following non-dimensional quantities can be defined:

$$t = \frac{t^* - t_c^*}{\tau^*}, \quad x_p = \frac{x_p^*}{l_1^*}, \quad \ell = \frac{l_2^*}{l_1^*},$$

$$c = \frac{c^*}{m^*}, \quad p = \frac{p^*}{\Delta p^*},$$

where c^* is the friction coefficient, t^* is the time, and t_c^* corresponds to the duration of the compression phase, which can be evaluated as:

$$x_p(0) = \int_{-t_c}^0 \dot{x}_p(t') dt' + 1. \quad (2)$$

In this equation, \dot{x}_p is the piston speed and $t_c = t_c^*/\tau^*$.

The mathematical model consists of three components, describing

- (i) the kinematics of the piston motion during the compression phase,
- (ii) the amplification of the turbulence and compositional fluctuations by piston-induced mean-strain, and
- (iii) the subsequent ignition of the test gas mixture under consideration of turbulence/chemistry interaction, wall-heat-loss effects, and detailed reaction chemistry.

These individual modeling components are discussed in the following sections.

2.1. Piston motion

The motion of the piston can be described by a second-order ordinary differential equation for a mass-spring-damping system. This equation is derived by applying a force balance on the freely moving piston:

$$\ddot{x}_p + p_{2,s} \left(\frac{\ell + 1 - x_p}{\ell} \right)^{-\gamma} - p_{1,s} x_p^{-\gamma} + c \dot{x}_p = 0. \quad (3)$$

The subscript “s” denotes the initial state at the beginning of the compression phase. The second and third term represent the pressure force acting on the piston, and the last term on the left-hand-side corresponds to the friction force. The pressure evolution in the driver and driven sections are derived from the isentropic state relation, in which the ratio of specific heats, γ , is assumed to be constant during the compression phase. This is accurate within $\pm 10\%$ for the species compositions and conditions considered here.

2.2. Flow field evolution during compression phase

The flow field in the driven section is characterized by the conservation equations for mass, momentum, species, and temperature, together with the ideal gas law. Using the references quantities l_1^* , τ^* , Δp^* , m^* , and A^* , the governing equations can be written in non-dimensional form as [22]:

$$D_t \rho = -\rho \nabla \cdot \mathbf{u}, \quad (4a)$$

$$\rho D_t \mathbf{u} = -\nabla p + \frac{1}{\text{Re}} \nabla \cdot \underline{\underline{\sigma}}, \quad (4b)$$

$$\rho D_t \mathbf{Y} = \frac{1}{\text{ReSc}} \nabla \cdot (\rho v \nabla \mathbf{Y}) + \rho \dot{\omega}, \quad (4c)$$

$$\begin{aligned} \rho c_p D_t T = & \text{Ec} D_t p + \frac{\text{Le}}{\text{ReSc}} \nabla \cdot (\lambda \nabla T) + \frac{1}{\text{ReSc}} \left(\rho v \sum_i c_{p,i} \nabla Y_i \right) \nabla T \\ & + \frac{\text{Ec}}{\text{Re}} \underline{\underline{\sigma}} : \nabla \mathbf{u} + \rho \dot{\omega}_T, \end{aligned} \quad (4d)$$

$$p = \frac{1}{\text{Ec}} \rho R T, \quad (4e)$$

where ρ is the density, \mathbf{u} is the velocity vector, $\underline{\underline{\sigma}}$ is the viscous stress tensor, v is the diffusivity, and $D_t = \partial_t + \mathbf{u} \cdot \nabla$ is the substantial derivative. The Reynolds number Re is defined in Eq. (1), the Schmidt number is $\text{Sc} = \nu^*/v^*$, the Lewis number is $\text{Le} = \lambda^*/(\rho^* c_p^* v^*)$, and $\text{Ec} = (l_1^*/\tau^*)^2 (c_p^* T^*)^{-1}$ is the Eckert number. The vector of species mass fractions and the corresponding production rates are denoted by \mathbf{Y} and $\dot{\omega}$, respectively; T is the non-dimensional temperature and $\dot{\omega}_T$ is the non-dimensional heat release rate.

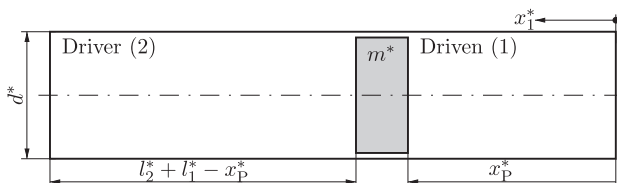


Fig. 1. Schematic of rapid compression machine. During the compression phase, the piston (gray) compresses the gas mixture in the driven section. The location of the piston is denoted by x_p^* ; mass of the piston is m^* , and initial length of the driver section is l_2^* . The diameter of the RCM is denoted by d^* .

2.2.1. Mean flow

Velocity, species mass fractions, and temperature are decomposed into a mean and a fluctuating quantity following the ensemble averaging procedure, viz. $\phi = \bar{\phi} + \phi'$. Since the Mach number is small, fluctuations in density can be neglected. It is assumed that the thermodynamic properties are not affected by variations in the composition. Furthermore, all viscous-diffusive properties are assumed to be constant during the compression phase. Under the assumption that the flow-field in the driven section is uni-directional, the mean velocity can be evaluated from the mean continuity equation and piston motion as:

$$\bar{u}_1 = \alpha(t) x_1 \quad \text{with} \quad \alpha(t) = \frac{\dot{x}_p(t)}{x_p(t)}, \quad (5)$$

where α is the time-dependent mean strain rate. The evolution of the mean mixture composition and temperature during the compression phase can be derived from Eqs. (4c) and (5):

$$\bar{\mathbf{Y}} = \langle \mathbf{Y} \rangle + \beta(t) \left(x_1 - \frac{x_p(t)}{2} \right) \quad \text{with} \quad \beta(t) = \beta_s \zeta(t), \quad (6)$$

where $\langle \cdot \rangle$ corresponds to a volume-averaged quantity, β_s denotes the stratification of the species composition at the beginning of the compression, and the compression ratio $\zeta(t)$ is evaluated as [23]:

$$\zeta(t) = \exp \left\{ - \int_{-t_c}^t \alpha(t') dt' \right\} = \frac{1}{x_p(t)}. \quad (7)$$

The temporal evolution of the mean pressure and temperature during the RCM compression phase are evaluated from the isentropic state relations:

$$\langle T \rangle(t) = \langle T_s \rangle \zeta(t)^{\gamma-1}, \quad (8)$$

$$\langle p \rangle(t) = \langle p_s \rangle \zeta(t)^\gamma. \quad (9)$$

The mean flow solution is then used to evaluate the amplification of turbulence and compositional fluctuations during the compression phase. For this, the rapid distortion theory is employed, and the derivation is discussed in the next section.

2.2.2. Turbulent flow field

Amplifications of turbulence and fluctuations in mixture composition are described using rapid distortion theory (RDT). RDT describes the evolution of initially homogeneous turbulence when it is subjected to rapid strain [23–25]. Specifically, RDT assumes that the evolution of the turbulence is controlled by the mean flow, and only weakly interacts with itself during the time over which the mean strain is applied. This can be characterized by the criterion

$$\frac{1}{\alpha} \frac{u'_s}{l_m} \ll 1, \quad (10)$$

where α is the characteristic mean strain rate (defined in Eq. (5)) and l_m/u'_s is the eddy life-time. Under these conditions, the non-linear terms in the fluctuating conservation equations can be neglected, and the resulting linearized equations can be written in index notation as:

$$\partial_i u'_i = 0, \quad (11a)$$

$$\partial_t u'_i + \alpha x_1 \partial_1 u'_i + \alpha u'_i \delta_{1i} = -\frac{1}{\rho} \partial_i p', \quad (11b)$$

$$\partial_t \mathbf{Y}' + \alpha x_1 \partial_1 \mathbf{Y}' + u'_i \beta = 0, \quad (11c)$$

$$\partial_t T' + \alpha x_1 \partial_1 T' = -(\gamma - 1) \alpha T'. \quad (11d)$$

Note that all viscous-diffusive contributions are neglected in deriving Eqs. (11), since they will only add an exponentially decaying coefficient in the RDT-formulation that is small compared to the strain-induced amplification rate. The temporal evolution of

the normal stresses and variance of species mass fractions and temperature is derived in Appendix A and is obtained as solution of the following equations:

$$\frac{\langle u_1^2 \rangle}{T_u^2} = \frac{3}{8\pi} \xi^2 \iint \frac{e_2^2 + e_3^2}{(e_1^2 \xi^2 + e_2^2 + e_3^2)^2} \sin \theta d\theta d\phi, \quad (12a)$$

$$\frac{\langle u_\alpha^2 \rangle}{T_u^2} = \frac{3}{8\pi} \iint \left\{ \frac{e_\alpha^2 e_1^2 (1 - \xi^2)}{(e_1^2 \xi^2 + e_2^2 + e_3^2)^2} \times \left[\frac{(1 - \xi^2)(1 - e_1^2)}{e_1^2 \xi^2 + e_2^2 + e_3^2} - 2 \right] + (1 - e_\alpha^2) \right\} \sin \theta d\theta d\phi, \quad (12b)$$

for $\alpha = \{2, 3\}$

$$\frac{\langle \mathbf{Y}^2 \rangle}{T_Y^2} = \frac{3}{8\pi} \frac{T_u^2}{T_Y^2} \beta_s^2 \iint J^2 (e_2^2 + e_3^2) \times \sin \theta d\theta d\phi + 1, \quad (12c)$$

$$\frac{\langle T^2 \rangle}{T_T^2} = \xi^{2(\gamma-1)}, \quad (12d)$$

where θ is the polar angle with $\theta \in [0, \pi]$, ϕ is the azimuthal angle with $\phi \in [0, 2\pi]$, $\mathbf{e} = (\cos\theta, \sin\theta\cos\phi, \sin\theta\sin\phi)^T$ is the unit wave number vector in spherical coordinates, and the term

$$J = \int_{-t_c}^0 \frac{\xi^2}{e_1^2 \xi^2 + e_2^2 + e_3^2} dt' \quad (13)$$

introduces a memory effect in Eq. (12c).

Equations (12) show that the amplification of the turbulence, scalar- and temperature-fluctuations during the RCM compression phase are directly dependent on turbulence intensity T_u , scalar fluctuations T_Y , temperature fluctuation T_T , mixture stratification β_s , and the compression ratio ξ . The parameters T_u , T_Y , and T_T are defined as:

$$T_u = u'_s \left(= u'_s \frac{T^*}{T_1} \right), \quad (14a)$$

$$T_Y = \mathbf{Y}'_s \left(= \mathbf{Y}'_s \right), \quad (14b)$$

$$T_T = T' \left(= \frac{T^*}{T} \right). \quad (14c)$$

2.3. Ignition and combustion phase

Following the compression phase, it is assumed that the combustion of the test gas mixture occurs through autoignition. The temporal evolution of the mixture is described by a Lagrangian Fokker–Planck model. This is a particle method and accounts for the interaction between turbulence, scalar mixing, and wall heat transfer.

In the absence of a mean flow, the decay of the homogeneous turbulence during the combustion phase is described by the evolution equations for the turbulent kinetic energy $\langle k \rangle = \frac{1}{2} \langle u_i^2 \rangle$ and dissipation rate $\langle \varepsilon \rangle$:

$$d_t \langle k \rangle = -\langle \varepsilon \rangle, \quad (15a)$$

$$d_t \langle \varepsilon \rangle = -C_{\varepsilon,2} \frac{\langle \varepsilon \rangle}{\tau_t} \quad \text{with} \quad \tau_t = \frac{\langle k \rangle}{\langle \varepsilon \rangle}, \quad (15b)$$

where $C_{\varepsilon,2}$ is a constant, and τ_t is the eddy life-time. The solution to Eqs. (15) can be described by a power-law decay as [23]:

$$\langle k \rangle = \langle k \rangle_0 \left(\frac{t}{\tau_0} + 1 \right)^{-n}, \quad \langle \varepsilon \rangle = \langle \varepsilon \rangle_0 \left(\frac{t}{\tau_0} + 1 \right)^{-(n+1)}, \quad (16)$$

and the subscript “0” denotes the condition at $t = 0$, corresponding to the end of the compression phase, and $\tau_0 = n \langle k \rangle_0 / \langle \varepsilon \rangle_0$. Using standard k - ε closure modeling, τ_0 and τ_t can be expressed as:

$$\tau_0 = \frac{n}{C_D} l_m \langle k \rangle_0^{-1/2}, \quad (17a)$$

$$\tau_t = \frac{1}{n} (t + \tau_0), \quad (17b)$$

where $\langle \varepsilon \rangle_0 = C_D \langle k \rangle_0^{3/2} l_m^{-1}$ was used [23,26]; n and C_D are constants, and l_m is a characteristic mixing length. These parameters are specified in Section 3.

The temporal evolution of the mixture is obtained from the solution of the LFP-model, which can be written as [27]:

$$d\boldsymbol{\psi} = \dot{\boldsymbol{\omega}} dt - \mathbf{a}(\boldsymbol{\psi}) dt + \mathbf{b}(\boldsymbol{\psi}) dW(t), \quad (18)$$

where $\boldsymbol{\psi} = (\mathbf{Y}, T)^T$ denotes the vector of the species mass fractions and temperature, and $\dot{\boldsymbol{\omega}}$ is the corresponding source term. The second term on the right-hand-side of Eq. (18) is the drift term, accounting for the interaction and micromixing among the ignition kernels. The last term is the diffusion term, and W denotes a Wiener process. It can be seen that in the limit of $\mathbf{a} \rightarrow 0$ and $\mathbf{b} \rightarrow 0$ the well-known homogeneous reactor model is recovered. As such, Eq. (18) can be considered as a first-order extension to the constant-volume homogeneous combustion problem.

The drift-term in Eq. (18) is modeled using the “interaction by exchange with the mean (IEM)” model [27], which is given as:

$$\mathbf{a} = \underline{\underline{A}} \begin{pmatrix} \mathbf{Y} - \langle \mathbf{Y} \rangle \\ T - \langle T \rangle \end{pmatrix} \quad \text{and} \quad \underline{\underline{A}} = \text{diag}(\tau_Y, (\tau_T + \tau_1))^{-1}. \quad (19)$$

By introducing the time scale ratios [28] $C_Z = \tau_t / \tau_Z$, $C_Y = \tau_Y / \tau_Z$, $C_T = \tau_T / \tau_Z$, and τ_t from Eq. (17b), $\underline{\underline{A}}$ can be written as:

$$\underline{\underline{A}} = \frac{C_Z}{C_Y} \frac{n}{(t + \tau_0)} \begin{pmatrix} \underline{\underline{I}} & \mathbf{0} \\ \mathbf{0} & \frac{C_Y}{C_T} \left(1 + \tau_1 \frac{C_Z}{C_T} \frac{n}{(t + \tau_0)} \right)^{-1} \end{pmatrix}, \quad (20)$$

where $\underline{\underline{I}}$ is the identity matrix, and C_Z , C_Y , and C_T are constants of order unity (specified in Table 1). Wall-heat-loss effects are incorporated in Eq. (19) through an adiabatic expansion model [29] by introducing the non-adiabatic core temperature $\langle T_1 \rangle$ and the thermal diffusion time scale τ_1 in Eq. (19). Details on the model formulation are presented in Section 2.4.

The term \mathbf{b} in Eq. (18) enforces that the diffusion process is constrained to the accessible state-space. This term is modeled as:

$$\mathbf{b}^2(\boldsymbol{\psi}) = \underline{\underline{A}} \begin{pmatrix} \langle \boldsymbol{\psi}^2 \rangle f(\boldsymbol{\psi}) \\ \langle T^2 \rangle f(T) \end{pmatrix} \quad (21)$$

with the shape function [27]:

$$f(\boldsymbol{\psi}) = \frac{(\boldsymbol{\psi} - \boldsymbol{\psi}^-)(\boldsymbol{\psi}^+ - \boldsymbol{\psi})}{\langle (\boldsymbol{\psi} - \boldsymbol{\psi}^-)(\boldsymbol{\psi}^+ - \boldsymbol{\psi}) \rangle}, \quad (22)$$

and $\boldsymbol{\psi}^\pm$ denotes the minimum and maximum value of a quantity $\boldsymbol{\psi}$ in the composition vector.

2.4. Consideration of wall-heat-loss effects

Effects of heat losses on the gas mixture during the ignition and combustion phase are accounted for in Eq. (18) through the non-adiabatic core temperature $\langle T_1 \rangle$. The calculation of this quantity follows the volume-expansion model of Tanaka et al. [29]. In the present formulation $\langle T_1 \rangle$ is obtained from the solution of the temperature equation, Eq. (4d), in which heat-flux contributions due to species diffusion and density gradients are neglected. The temperature profile in the boundary layer can then be obtained from the solution of the energy equation, which is here written in polar coordinates as:

$$\partial_t \Theta = (1 - \Theta) d_t \ln \langle T \rangle - T_w + \frac{\text{Le}}{\text{ReSc}} \frac{1}{r} \partial_r (rv \partial_r \Theta), \quad (23)$$

where r is the radius, T_w is the wall temperature, $\langle T \rangle$ is obtained from the LFP solution, and Θ is the normalized temperature, which is defined as:

$$\Theta = \frac{T - T_w}{\langle T \rangle - T_w}. \quad (24)$$

The boundary conditions for Eq. (23) are:

$$\text{Adiabatic core region: } \partial_r \Theta|_{r=0} = 0, \quad (25)$$

$$\text{Isothermal wall: } \Theta|_{r=d/2} = 0. \quad (26)$$

With the time-dependent solution of Eq. (23), the non-adiabatic core temperature can then be computed as:

$$\langle T \rangle = (\langle T \rangle - T_w) \frac{8}{d^2} \int_0^{d/2} \Theta r dr + T_w. \quad (27)$$

The displacement thickness of the thermal boundary layer is:

$$\delta_1 = \int_0^{d/2} (1 - \Theta) dr, \quad (28)$$

so that the thermal diffusion time scale can then be evaluated as $\tau_1 = \delta_1^2/\nu$.

2.5. Model implementation

In the following, the implementation of the RCM model is summarized and numerical details regarding the solution approach are provided.

Starting with the RCM-compression phase, Eq. (3) is integrated to obtain the piston motion and time-dependent strain rate. Input parameters for Eq. (3) are the pressures in and geometric dimensions of the driver and driven sections. With the solution for the piston location, $\zeta(t) = 1/x_p(t)$, the RDT-equations are solved to specify the state of the mixture at the end of the compression phase, which is defined by the quantities $\langle k \rangle/T_u^2$, $\langle \mathbf{Y}^{\prime 2} \rangle/T_u^2$, and $\langle T^{\prime 2} \rangle/T_u$. From these statistical quantities and parametric information about turbulence levels and stratification, the stochastic particles in the LFP-model are initialized.

The thermochemical composition of all particles is sampled from probability density functions (PDFs) with prescribed mean and variance. Specifically, the temperature field is initialized from a Gaussian distribution, and a beta-distribution is used for sampling the initial mixture composition. The particles are advanced by solving Eq. (18) using the drift and diffusion terms given in Eqs. (19) and (21), respectively. During the combustion phase, the decay of the turbulence is described by Eq. (16), and the turbulent kinetic energy that was computed at the end of the compression phase enters the LFP model through the time scale τ_0 (see Eq. (17a)) via the drift matrix \underline{A} . In this time-explicit method, the boundary layer thickness and thermal diffusion time τ_1 are computed from information at the previous time step. The detailed chemistry is either directly coupled through CHEMKIN-libraries [30] (Section 4.3) or precomputed and tabulated to increase computational efficiency (Section 4.4). The LFP-code is fully parallelized using the MPI-paradigm, and 20,000 particles are used in all simulations.

Table 1
Model constants for RCM-model.

n	C_D	C_Z	C_T	C_V	l_m
1.3	0.1664	2.0	1.0	1.0	0.0259

3. Specification of model configuration

The compression-ignition model, that was developed in the previous sections, is applied to the free-piston RCM at the University of Michigan [21]. The UM-RCM facility consists of a pressurized driver section having a length of 5.54 m and an inner diameter of 154 mm. The driven section, containing the test gas mixture, is separated from the driver section through a freely moving piston. The driven section is 2.54 m long and has an inner diameter of 101.2 mm. The end of the driven section is connected to the test section with an inner diameter of 50.8 mm and a length of 50.6 mm. In the following, the geometry of the UM-RCM facility is modeled as cylinder having a constant diameter, and the dimensions are corrected to reproduce the geometric compression ratio of the facility. The length of the driven section, including the test section, is $l_1^* = 2970$ mm, the length of the test section is 77 mm, resulting in a compression ratio of $\xi = 38.6$. The diameter of all sections is kept constant and equal to that of the UM-RCM with 101.2 mm. The mass of the piston is $m^* = 2.575$ kg, the pressure in the driver section is $p_{2,s}^* = 2.0735$ bar, and friction is neglected. The initial pressure in the driven section is $p_{1,s}^* = 0.097$ bar and the ratio of specific heats is $\gamma = 1.3$. Note that the cross-section area and the mass of the piston only affect the reference time scale τ^* , which is evaluated to be $\tau^* = 69.36$ ms.

The test gas in the driven section consists of a fuel-lean syngas/air mixture. Different syngas mixtures, with the composition:

$$\phi(v_{H_2}H_2 + CO) + v_{CO_2}CO_2 + v_{O_2}O_2 + v_{N_2}N_2 \quad (29)$$

are considered. In this equation, v_i is the stoichiometric coefficient of species i ; ϕ is the equivalence ratio, which can be expressed in terms of the mixture fraction Z and its stoichiometric value Z_{st} [28]:

$$\phi = \frac{Z}{Z_{st}} \frac{1 - Z_{st}}{1 - Z}. \quad (30)$$

The chemical mechanism by Li et al. [31] is used to describe the syngas combustion, and all model constants used in the LFP model are summarized in Table 1.

4. Results

4.1. RCM compression phase

The temporal evolution of piston location, piston velocity, and mean strain rate are illustrated in Fig. 2. Note that the time and all other quantities are non-dimensionalized, and $t = 0$ corresponds to the end of the compression phase. From this figure, it can be seen that the piston exhibits an approximately constant acceleration up to $t = -0.35$, after which the piston decelerates due to the compression of the test gas mixture in the driven section.

The mean strain rate, shown in Fig. 2c, remains small up to $t = -0.35$. However, beyond this point α rapidly increases in magnitude until it reaches a value of -39.5 at the end of the compression phase.

4.2. Turbulence amplification during compression phase

The temporal evolution of the turbulence and compositional fluctuations during the RCM compression phase are shown in Fig. 3. From this figure, it can be seen that all turbulent quantities remain approximately constant and equal to their initial values up to $t = -0.35$. Beyond this point a nearly exponential increase in the turbulence quantities is observable, which is associated with the rapid increase in the strain rate (see Fig. 2c). Physically, the turbulence amplification can be understood as result of the mean-flow

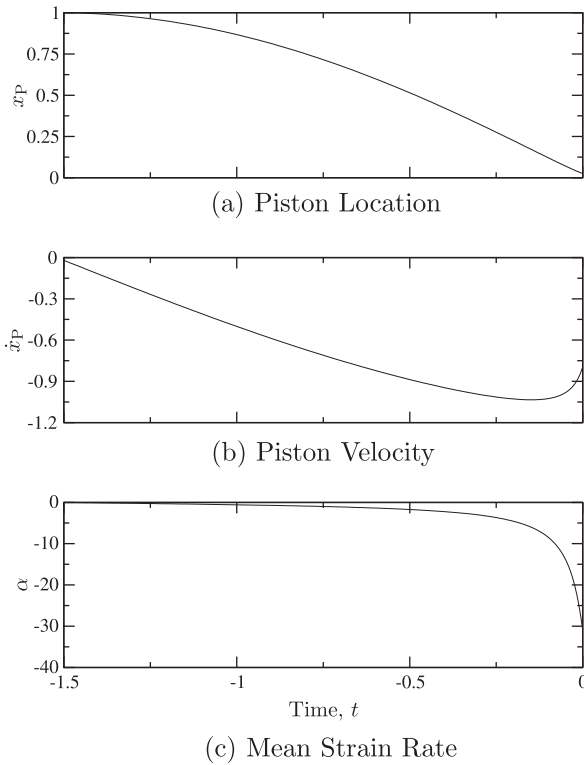


Fig. 2. Kinematics of the RCM-facility during the compression phase, showing (a) piston location x_p , (b) piston velocity \dot{x}_p , and (c) mean strain rate $\alpha = \dot{x}_p/x_p$.

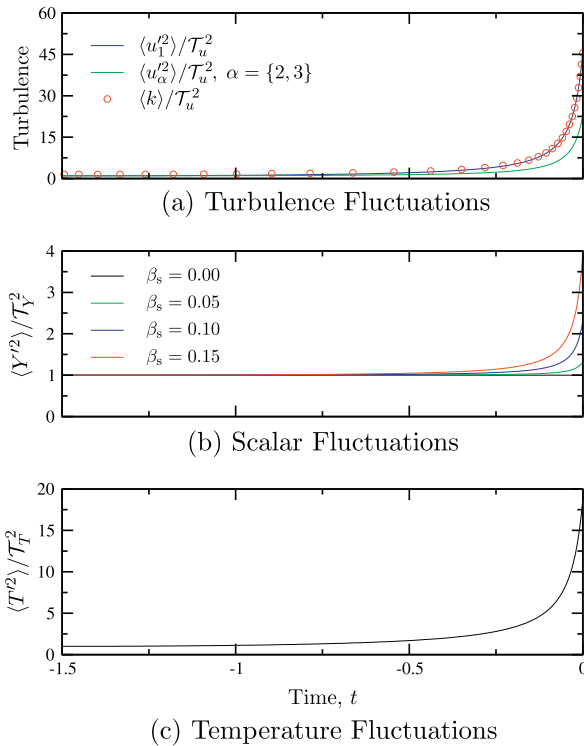


Fig. 3. Temporal evolution of (a) turbulence and fluctuations in (b) composition and (c) temperature during the RCM-compression phase.

induced distortion of turbulent eddies and the corresponding increase in Reynolds stresses [25].

The evolution of the scalar variance for different values of mixture stratification is shown in Fig. 3b. Since $\langle Y^2 \rangle$ has a

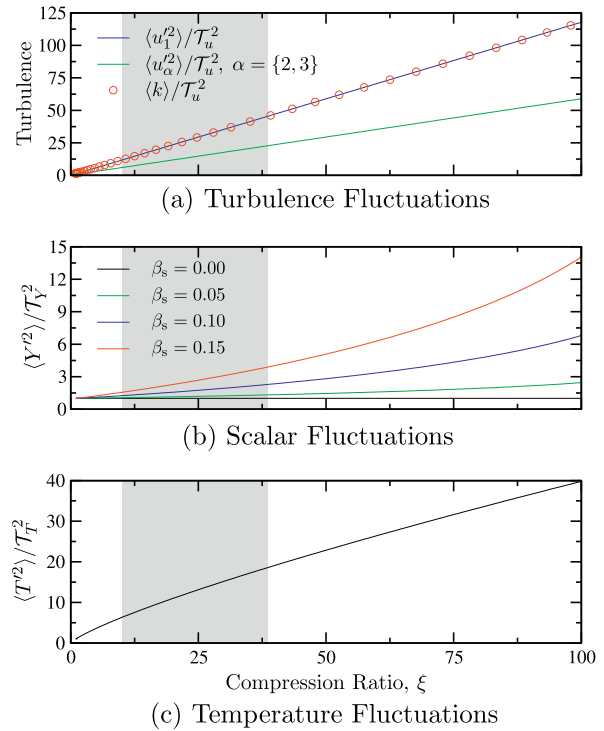


Fig. 4. Amplification of turbulence quantities as function of compression ratio, showing (a) turbulent normal stresses and turbulent kinetic energy, (b) amplification of the scalar variance for different values of initial mixture stratification, and (c) amplification of temperature variance. The region in gray illustrates the typical range of RCM compression ratios.

quadratic dependence on β_s (see Eq. (12c)), scalar fluctuations are amplified due to the mean stratification. Although not further considered in the present work, it is noted that such mean stratification effects could become of potential importance when an internal mixture preparation is facilitated.

Since RCM-facilities employ different compression ratios, we will next investigate how the compression ratio affects the turbulence production during the compression phase. For this, additional calculations are performed in which the compression ratio is extended up to $\xi = 100$. Results of this analysis are presented in Fig. 4; for reference, the gray area in this figure indicates the typical range of RCM compression ratios. Figure 4a shows the dependence of the normal stresses and the turbulent kinetic energy on the compression ratio. Note that the turbulence level in the driven section is only a function of turbulence level T_u and compression ratio, but – unlike the scalar fluctuations – is not affected by the temporal evolution of the compression phase. Following an initial transition, all normal stress components are linearly dependent on the compression ratio. Due to the rapid straining, the initially isotropic turbulence field transitions to anisotropy, in which the $\langle u_1^2 \rangle$ -component is growing fastest and exceeding the other components by a factor of two.

The results from this RDT analysis are particularly interesting, since they reveal the sensitivity of the turbulence level at the end of the RCM-compression phase to the mean-strain amplification. Specifically, Fig. 4 shows that for RCM-facilities with compression ratios as high as 40 the turbulence is amplified by as much as a factor of 50. The reader is reminded that in this work different turbulence contributions are parametrically represented in terms of an initial turbulence level. Despite this simplification, these results indicate that the piston-induced mean-strain is a relevant mechanism in enhancing the fluctuations in the test gas mixture at the end of the compression phase. In conjunction with Fig. 3

it can also be conjectured that turbulence-generating mechanisms that evolve throughout the compression phase (such as wall-generated turbulence and the formation of corner vortices) will also be affected by the compressive strain, which is mainly prevailing during the later stage of the compression phase.

4.3. Effects of temperature fluctuations and wall heat losses

The objective of this section is to analyze the coupling between turbulence, temperature fluctuations, and wall heat losses in the absence of compositional variations of the test-gas mixture. Recently, Mittal & Sung performed acetone-PLIF measurements to characterize the temperature field in a RCM-facility. They reported root-mean-square (rms) temperature fluctuations around 25 K and measured instantaneous peak temperature fluctuations as large as 100 K after compression for a RCM with a geometric compression ratio of 15.1 [12]. These temperature inhomogeneities are generated by the mixing between fluid in the colder boundary layer and the test gas mixture in the core region during the compression. In the present formulation, these multidimensional mixing processes are not explicitly modeled, so that temperature fluctuations at the end of the compression phase are directly represented through the parameter \mathcal{T}_T and the mean compression temperature $\langle T^* \rangle$. Therefore, Eq. (12d) is not solved, and the reader should associate \mathcal{T}_T with the temperature perturbations at the beginning of the ignition phase.

To quantify the role of temperature perturbations on the ignition dynamics, the mixture composition is kept constant, and the temperature of all particles is initialized from a Gaussian distribution with mean $\langle T^* \rangle$ and variance $(\mathcal{T}_T \langle T^* \rangle)^2$.

Simulation results for different levels of initial temperature fluctuations, \mathcal{T}_T , are presented in Fig. 5. For these calculations, the initial turbulence level is kept constant with $\mathcal{T}_u = 0.1$. The mixture composition is $\text{H}_2/\text{O}_2/\text{CO}_2/\text{O}_2/\text{N}_2 = 7.33/9.71/1.98/17.01/63.97$ with $\phi = 0.5$, and pressure and temperature at the end of the compression phase are $\langle p^* \rangle = 20$ bar and $\langle T^* \rangle = 850$ K. The wall temperature is set equal to 90% of the mean temperature at the end of the compression phase. Solid lines indicate adiabatic results, and non-adiabatic simulations are shown by dashed lines.

The results show that the initial temperature fluctuations have a direct effect on the onset of the ignition, and with increasing levels of \mathcal{T}_T the ignition time reduces. It can also be seen that the slope of the pressure and temperature traces decrease with increasing levels of initial temperature fluctuation. This is in qualitative agreement with experimental results which are included for comparisons in Fig. 5a.

Comparisons between adiabatic and non-adiabatic simulations show that for these operating conditions wall heat losses are secondary in affecting the onset of ignition. While wall heat losses typically lead to a delay in τ_{ig} , it is interesting to point out that non-adiabatic conditions can also have an opposite effect, as evident for the case with $\mathcal{T}_T = 0.05$ (see green¹ lines in Fig. 5). For this condition the heat loss favors a slightly earlier ignition which is opposite to the homogeneous reactor simulation and configurations with higher turbulence levels.

The evolution of the rms temperature is presented in Fig. 5c, showing that the location of the peak temperature fluctuation directly correlates with the ignition delay time, which is commonly associated with the location of the steepest pressure slope:

$$\tau_{\text{ig}} = \{t | d_t(p^*)(t) \rightarrow \max\}. \quad (31)$$

Beyond this ignition point the temperature fluctuations rapidly de-

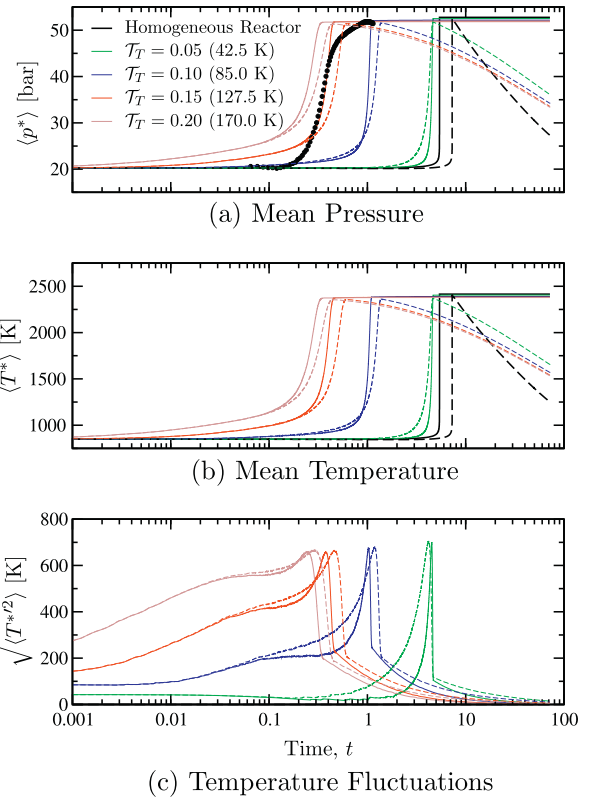


Fig. 5. Evolution of (a) mean pressure, (b) mean temperature, and (c) temperature fluctuations for different values of temperature perturbations \mathcal{T}_T and fixed turbulence level of $\mathcal{T}_u = 0.1$; corresponding temperature fluctuations at the end of the compression phase are given in parentheses. The mixture composition is $\text{H}_2/\text{O}_2/\text{CO}_2/\text{O}_2/\text{N}_2 = 7.33/9.71/1.98/17.01/63.97$ and $\phi = 0.5$; pressure and temperature at the end of the compression phase are $\langle p^* \rangle = 20$ bar and $\langle T^* \rangle = 850$ K, respectively. Solid lines correspond to adiabatic results and dashed lines show results with wall heat losses. Pressure-corrected measurements for the same mixture composition are shown by closed symbols [5].

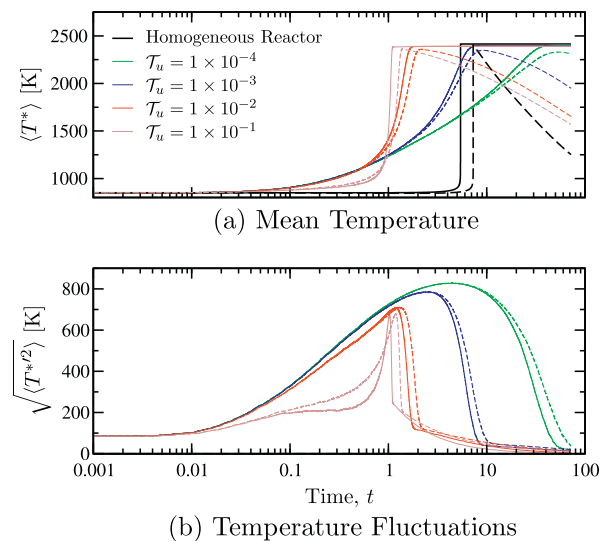


Fig. 6. Evolution of (a) mean temperature and (b) temperature fluctuations for different levels of turbulence \mathcal{T}_u and fixed temperature perturbation of $\mathcal{T}_T = 0.1$. The mixture composition is $\text{H}_2/\text{O}_2/\text{CO}_2/\text{O}_2/\text{N}_2 = 7.33/9.71/1.98/17.01/63.97$ and $\phi = 0.5$; pressure and temperature at the end of the compression phase are $\langle p^* \rangle = 20$ bar and $\langle T^* \rangle = 850$ K, respectively. Solid lines correspond to adiabatic results and dashed lines show results with wall heat losses.

¹ For interpretation of color in Figs. 3–11, the reader is referred to the web version of this article.

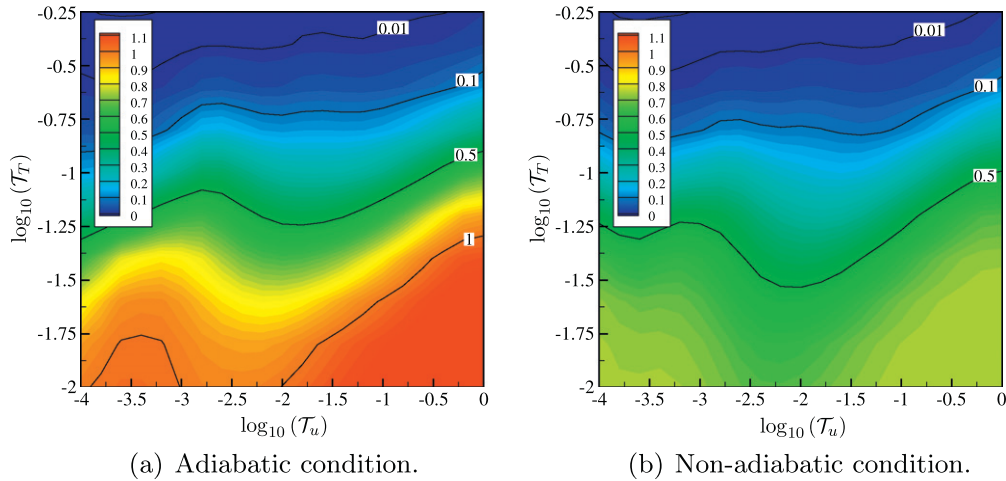


Fig. 7. Ratio of ignition delay times between LFP-model and homogeneous reactor solution, τ_{ig}/τ_{ig}^{HR} , as function of turbulence intensity and temperature fluctuations: (a) adiabatic and (b) non-adiabatic conditions. The mixture composition is $H_2/O_2/CO_2/O_2/N_2 = 7.33/9.71/1.98/17.01/63.97$ and $\phi = 0.5$; pressure and temperature at the end of the compression phase are $\langle p^* \rangle = 20$ bar and $\langle T^* \rangle = 850$ K, respectively.

cay and the products reach a uniform composition.

Since in the present model the ignition process is controlled by the turbulence evolution, we will next analyze effects of different turbulence levels on the ignition dynamics of the mixture. To this end, simulations are performed for increasing levels of turbulence and keeping the temperature fluctuations constant with $\mathcal{T}_T = 0.1$. Results of this parametric study are illustrated in Fig. 6. It can be seen that very low turbulence levels lead to extended ignition processes, which is reflected by large temperature fluctuations. The reduced turbulence level \mathcal{T}_u increases the turbulence time scale τ_0 ($\tau_0 \propto \mathcal{T}_u^{-1}$, see Eq. (17a)), resulting in a suppressed micromixing, so that individual ignition kernels evolve in isolation without significant interaction with their respective environments. With increasing turbulence levels, the heat transfer from hot to cold ignition kernels is enhanced resulting in faster ignition of the entire mixture. Note that for the conditions considered here, the heat release exceeds the heat loss by turbulent mixing so that quenching is not relevant.

By considering both parametric dependencies, the ignition delay time as function of \mathcal{T}_u and \mathcal{T}_T can be evaluated. This is illustrated in Fig. 7, showing the ratio of the ignition delay times between LFP-model and homogeneous reactor solution, τ_{ig}/τ_{ig}^{HR} . The results of this parametric study show that – in the absence of compositional inhomogeneities – initial perturbations in temperature have a direct effect on reducing the ignition delay, irrespectively of adiabatic or non-adiabatic operating conditions; wall heat loss only lead to a shift to lower values of \mathcal{T}_T . From Fig. 7 it can also be seen that for low values of \mathcal{T}_T the turbulence can either reduce or increase the ignition delay. This can be attributed to the interaction between turbulence and chemistry, and will be further discussed in the context of a Damköhler analysis in Section 4.5.

4.4. Compositional variations of test gas mixture

Effects of turbulence and compositional variations on the ignition behavior are investigated next. To this end, we will focus on the adiabatic formulation. Under this condition the LFP-model can be reduced to a two-scalar problem in which the temporal evolution of the mixture can be fully described by the mixture fraction Z and a reaction progress variable C . With this, the state-vector in Eq. (18) takes the form $\psi = (Z, C)^T$, and the progress variable is defined from a linear combination of major product mass fractions,

$C = Y_{CO_2} + Y_{CO} + Y_{H_2O} + Y_{H_2}$. This formulation allows for precomputing the reaction chemistry prior to the LFP-computation and tabulating all thermochemical quantities in terms of Z and C . Using this formulation, the LFP model is solved for a range of turbulence intensities \mathcal{T}_u and initial mixture fraction fluctuations \mathcal{T}_Z . The mixture is selected from Ref. [5], having the following composition: $H_2/CO/CO_2/O_2/N_2 = 6.7/4.5/12.2/18.7/57.9$ and $\phi = 0.3$. The temperature and pressure at the end of the compression phase are $\langle T^* \rangle = 944$ K and $\langle p^* \rangle = 11.2$ bar, respectively. For the present case, the mean mixture stratification is set to zero. The mixture composition is initialized from a beta-distribution [28]:

$$P(Z; \langle Z \rangle, \mathcal{T}_Z^2) = \frac{\Gamma(\alpha + \beta)}{\Gamma(\alpha)\Gamma(\beta)} Z^{\alpha-1} (1-Z)^{\beta-1} \quad (32)$$

in which the coefficients α , β , and γ are expressed in terms of $\langle Z \rangle$ and \mathcal{T}_Z^2 :

$$\alpha = \langle Z \rangle \gamma, \quad \beta = (1 - \langle Z \rangle) \gamma, \quad \gamma = \frac{\langle Z \rangle (1 - \langle Z \rangle)}{\mathcal{T}_Z^2} - 1. \quad (33)$$

The progress variable for each particle is determined from the mixture composition for Z and the condition at the end of the compression phase.

Results for the temporal evolution of mean pressure and temperature are illustrated in Fig. 8. It can be seen that the LFP model agrees with the homogeneous reactor results (open symbols) for extremely small values of initial turbulence and scalar fluctuations, but deviates with increasing values of \mathcal{T}_u and \mathcal{T}_Z . Higher turbulence levels lead to a successive reduction in ignition delay. For this particular mixture composition the reduction in ignition delay can reach an order of magnitude for $\mathcal{T}_u = 10^{-3}$. In this context it is noted that this value of \mathcal{T}_u corresponds to rms velocity fluctuations of 0.4 m/s at the end of the compression phase, which is more than an order of magnitude smaller compared to the measurements by Guibert et al. [14]. Such values appear to be reasonable, and belong to the lower turbulence regime for in-cylinder flows [16,32].

From these results it is also evident that the turbulence not only affects the onset of the ignition but also the progress of reaction. Compared to the homogeneous reactor results, the rise in pressure and temperature reduces with increasing perturbation levels. This behavior is qualitatively similar to measurements, and is illustrated by the experimental data in Fig. 8 [5,33]. The operating condition and mixture composition is identical to that used for the simulations, and the model results show a similar trend. Note that

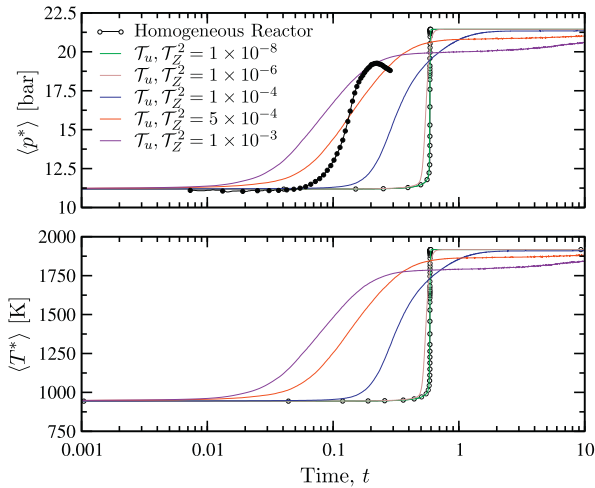


Fig. 8. Evolution of mean pressure (top) and temperature (bottom) for different values of turbulence and scalar fluctuations. Open symbols correspond to homogeneous reactor results and the experimentally recorded pressure-history is shown by closed symbols [5] for qualitative comparisons. The mixture composition is $H_2/O_2/CO_2/O_2/N_2 = 6.7/4.5/12.2/18.7/57.9$ and $\phi = 0.3$; pressure and temperature at the end of the compression phase are $\langle p^* \rangle = 11.2$ bar and $\langle T^* \rangle = 944$ K, respectively.

this allows only for a qualitative comparison since the degree of inhomogeneities in the test gas mixture was not measured, and effects other than compositional fluctuations could also be responsible for this ignition behavior.

To complete this ignition analysis, we will assess the role of perturbations in the species composition on the ignition behavior. To this end, T_z is set to zero, so that all particles are initialized with the same mixture fraction. To account for small-scale variations in species composition, small perturbations in C are added to the progress variable. These fluctuations are sampled from a uniform distribution, and its rms-value is denoted by T_C .

Results obtained from a parametric study are presented in Fig. 9, showing the computed pressure traces for different values of T_u . Results shown by the dash-dotted lines are obtained for $T_C = 2 \times 10^{-5}$, solid lines for $T_C = 2 \times 10^{-4}$, and the dashed lines correspond to $T_C = 4 \times 10^{-4}$. From this figure the following observations can be made. First, it is seen that the onset of ignition is primarily controlled by the progress variable fluctuations, and turbulence plays only a secondary role in determining the ignition point. This observation is noteworthy as it is of direct relevance for practical applications. For instance, RCMs employing external mixture preparation establish very homogeneous compositions and negligible variations in equivalence ratio. However, wall heat transfer, mixture impurities, or surface-catalytic effects can result

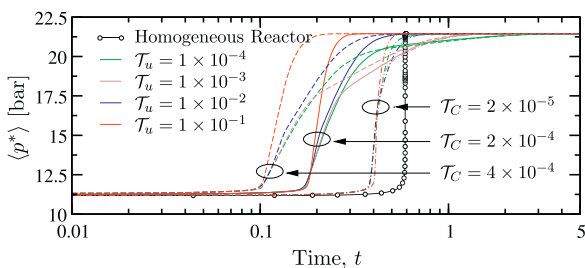


Fig. 9. Evolution of mean pressure for different values of initial turbulence (indicated in the legend) and three different values of T_C ; Dash-dotted lines: $T_C = 2 \times 10^{-5}$; solid lines: $T_C = 2 \times 10^{-4}$; and dashed lines: $T_C = 4 \times 10^{-4}$. The mixture composition is $H_2/O_2/CO_2/O_2/N_2 = 6.7/4.5/12.2/18.7/57.9$ and $\phi = 0.3$; pressure and temperature at the end of the compression phase are $\langle p^* \rangle = 11.2$ bar and $\langle T^* \rangle = 944$ K, respectively.

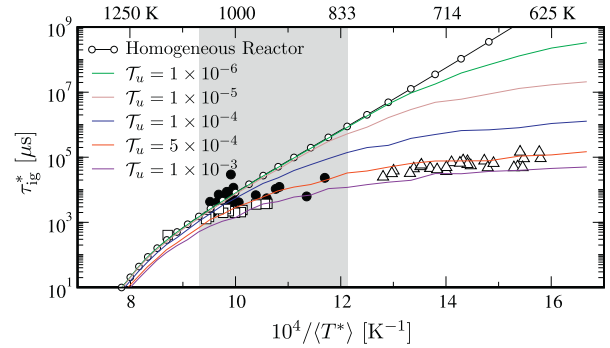


Fig. 10. Ignition delay time of syngas/air mixtures. Experimental data are corrected to 20 atm assuming $1/\langle p^* \rangle$ proportionality [6]. Symbols correspond to: RCM \bullet [5]; ST \square [6]; FR \triangle [34]. Mixture composition is $H_2/CO/CO_2/O_2/N_2 = 7.33/9.71/1.98/17.01/63.97$ and $\phi = 0.5$; pressure at the end of the compression phase is $\langle p^* \rangle = 20$ atm; grey area illustrates the typical RCM-operating range.

in small compositional variations and therefore affect the ignition delay. The second observation relates to the slope of the pressure rise. From this parametric study it is evident that with increasing turbulence intensity the reaction progress is delayed. In fact, it appears that for the case with $T_u = 1 \times 10^{-3}$ combustion proceeds as a two-stage process which is reflected by a reduced pressure rise after about 60% of the maximum pressure is reached.

4.5. Syngas ignition and combustion

The ignition analysis is further extended and effects of initial turbulence and equivalence ratio fluctuations on the ignition delay over a temperature range of $600 \text{ K} \leq \langle T^* \rangle \leq 1300 \text{ K}$ are investigated.

Modeling results and comparisons with experimental data for ignition delay times are shown in Fig. 10. Results from the RCM model (lines) show that effects of turbulence are mainly pronounced at low temperatures, which is evident from the results with $T_u = T_z^2 = 1 \times 10^{-6}$ (green line in Fig. 10). However, with increasing levels of turbulence and mixture fluctuations, ignition delay times at higher temperatures become increasingly affected. This can be explained through a Damköhler number analysis, comparing the characteristic turbulence time scale with the ignition delay time:

$$Da_{ig} = \frac{\tau_0^*}{\tau_{ig}^*} \propto \frac{1}{\xi^{3/2}} \frac{1}{T_u} \frac{\tau^*}{\tau_{ig}^*} \quad (34)$$

Large values of Da_{ig} identify ignition-dominated processes which are unaffected by turbulent mixing.

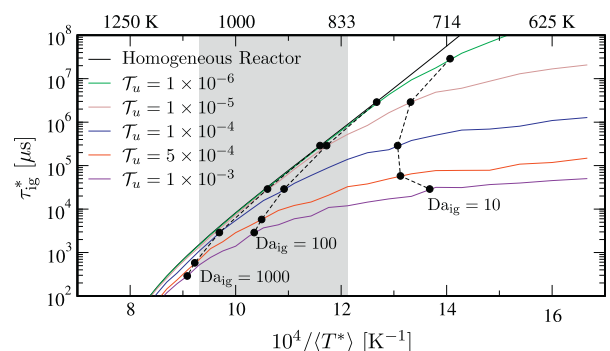


Fig. 11. Damköhler number criterion for syngas ignition analysis. Mixture composition and operating conditions are the same as in Fig. 10. Dashed lines with symbols correspond to curves of constant Damköhler numbers, $Da_{ig} = \{10, 100, 1000\}$.

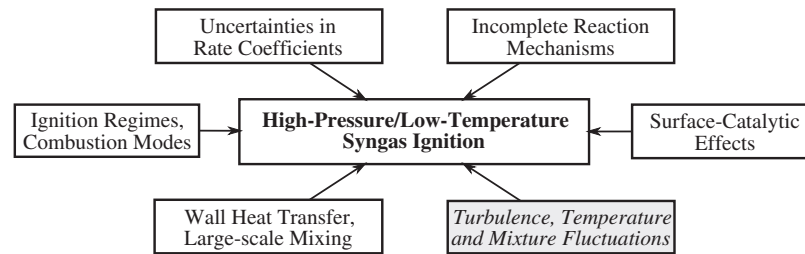


Fig. 12. Chemical-kinetics and hydrodynamic processes affecting the syngas ignition at high-pressure/low-temperature conditions.

The Damköhler number is evaluated from the simulation results, and is illustrated in Fig. 11. Isocontours for three values of Da_{ig} are shown. It can be seen that all ignition delay curves converge for $Da_{ig} \geq 100$ and asymptote to the homogeneous reactor results. This analysis suggests that Eq. (34) can be utilized as criterion to assess the significance of turbulent mixing and mixture fluctuations on the ignition process.

The RCM model parametrically captures the experimentally observed trend that the ignition delay time asymptotes to a constant value around 100 ms for low mixture temperatures (see Fig. 10). Although the data for $(T^*) < 800$ K are obtained from flow reactor experiments, the proposed model predicts a similar behavior. This suggests that turbulence effects could also be of relevance in flow reactors, and further research is required to confirm this hypothesis.

5. Discussion

A parametric study was performed to investigate effects of turbulence, fluctuation in mixture composition and temperature, and wall heat transfer on the ignition dynamics of lean syngas mixtures in RCMs. The state of the test gas at the end of the compression phase was evaluated by considering the mean-strain induced amplification of turbulence and compositional perturbations during the piston compression. Turbulence-generating mechanisms and compositional variations of the test-gas mixture are parametrically represented by the turbulence intensity T_u and fluctuations in composition and temperature, T_V and T_T , respectively. As such, this model can be used for investigating ignition sensitivities to relevant process parameters and operating conditions. The fidelity of this low-order model can be enhanced by injecting facility-specific information about turbulence levels and mixture inhomogeneities that are either obtained from measurements or detailed simulations. The ignition of the syngas mixture is modeled as a stochastic process. This formulation, which reduces to the homogeneous reactor model in the absence of turbulence and perturbations in mixture composition and temperature, accounts for the micromixing among different ignition environments. The current model formulation considers the volumetric ignition regime, and only incompletely characterizes front-like combustion modes [5,14,15]. However, such effects can be incorporated in the RCM ignition model. In this regard it is noted that this model can also be of relevance for application to homogeneous and stratified charge compression ignition (H/SCCI) in internal combustion engines [35]. In these advanced engine concepts, thermal and mixture inhomogeneities are present, resulting in sequential ignition of the mixture and the presence of deflagrative and front-like combustion regimes [36,37].

In the previous section, a Damköhler criterion was introduced to quantify the role of turbulence on the ignition process. It was shown that with decreasing values of Damköhler number (corresponding to decreasing temperature), turbulence and mixture fluctuations become increasingly effective in controlling the induction

chemistry. This suggests that turbulence/chemistry interaction can become of equal importance as chemical-kinetics and hydrodynamics processes which have been previously identified as key mechanisms [3,38] for the observed discrepancies between measured and computed ignition delay times. These mechanisms are schematically summarized in Fig. 12. The identified dependency of the low-temperature syngas ignition to turbulence and mixture inhomogeneities requires the careful control and characterization of RCM-operating conditions. With a few exceptions of measurements during the ignition process [14], the experimental characterization of turbulence and compositional perturbations before and during the compression phase have not been performed, and are of interest for future model comparison. Such measurements would also be helpful in delineating facility-specific turbulence contributions arising from the mixture-preparation and filling processes, boundary-layer generated turbulence, and corner-vortices.

Currently the significance of the turbulence on the ignition process in RCMs is not fully appreciated so that CFD studies have been typically performed under laminar conditions [10,39]. Although an important first step, such simulations only provide an incomplete description of the flow field structure, and caution must be exercised when these results are compared with zero-dimensional models and measurements. In this context it is also noted that laminar or ensemble-averaged RANS (Reynolds-averaged Navier–Stokes) calculations in combination with equilibrium turbulence closure models appear to be inappropriate for RCM-simulations for at least two reasons. First, the strong mean strain, generated by the rapid piston motion, results in the generation of non-equilibrium turbulence. Since standard k - ϵ turbulence models are derived from equilibrium arguments, the Reynolds-stresses are considerably over-predicted. This represents a limitation of standard two-equation models, and Reynolds-stress models will most-likely provide improved predictions for the non-equilibrium turbulence amplification in RCMs. The second concern addresses the description of the ignition and combustion processes. The ignition process in RCMs evolves on sub-millimeter scales and is typically not resolved in laminar/RANS CFD calculations. Because of these modeling challenges, it is speculated that detailed unsteady simulations with adequate resolution of small-scale ignition processes and turbulence/chemistry interaction are required to provide a quantitative description of the flow field structure and combustion in RCMs.

6. Conclusions

The role of turbulence on the syngas ignition in rapid compression machines over a wide range of operating conditions was studied. For this, a self-contained model was developed that describes the amplification of small-scale turbulence and mixture fluctuations during the RCM compression phase and the subsequent ignition process. Rapid distortion theory is utilized to characterize the turbulence amplification during the compression phase. The ignition process is described by a Lagrangian Fokker–Planck model, which

considers the micromixing between different ignition environments. The model reduces to the well-known homogeneous reactor problem in the absence of perturbations in the initial flow field, mixture composition, and temperature. The model analysis showed that the turbulence level \mathcal{T}_u , temperature perturbations \mathcal{T}_T , mixture fluctuation \mathcal{T}_Y , mean mixture stratification β_s , and compression ratio ξ are the key parameters that affect the ignition process.

Comparisons with experimental data showed that the model parametrically captures observed trends of retarded reaction progress and reduced ignition delay for increasing levels of turbulence and mixture fluctuations. Parametric studies were conducted for different turbulence and mixture conditions over a wide range of operating conditions. In this study, a Damköhler criterion was proposed to characterize the sensitivity of the induction chemistry to turbulence and mixture fluctuations in RCMs. Mixtures with Damköhler numbers below a value of approximately 50 exhibit increasing sensitivities to turbulence fluctuations which is reflected by significant reduction in ignition delay times.

Although this study only considered an idealized RCM-facility and syngas-mixture, based on these modeling results the following recommendations can be made to further assess the relevance of nonidealities in rapid compression machines:

- Parametric studies identified turbulence and fluctuations in temperature and composition as potential sources for systematic errors in RCM-measurements. These errors are presumably dependent on operating conditions and facility-specific, and could exacerbate other non-idealities that arise from heat-transfer, mixture impurities, catalytic effects, among others.
- Detailed measurements of turbulence and flow-field structure throughout the compression stroke and ignition phase are desirable to improve the quantitative understanding about inhomogeneities that arise from hydrodynamic processes. Such measurements are also helpful to further constrain the parameters in the RCM-model.
- Depending on the Damköhler criterion, the turbulence/chemistry interaction could add a stochastic component to the RCM-ignition process. This would require multiple experiments to obtain statistically significant results and quantify experimental uncertainties.
- Model results suggest that comparisons of global quantities, such as ignition delay and equilibrium composition, remain relatively insensitive to facility-induced perturbations. Therefore, time-resolved measurements for temperature, pressure, speciation, and wall-heat flux would be desirable to enable a systematic comparison with computational models and high-fidelity simulations.

Acknowledgments

This work was supported in part by the Office of Naval Research under Award No. N00014-10-1-0561, the Air Force Office of Scientific Research under Award No. FA9550-11-1-0031, and the Department of Energy under Grant DE-FE0007060. We would like to express our gratitude to Margaret Wooldridge and Darshan Karwat for sharing their experimental data. The assistance of Simon Weiher for conducting simulations in support of this investigation is gratefully acknowledged.

Appendix A. Derivation of RDT-equations

In the following, the key steps in deriving Eqs. (12) are summarized. The derivation follows standard RDT-formulation [23,26]. Beginning with Eqs. (11), all fluctuating quantities are expressed in terms of a Fourier mode:

$$\phi' = \hat{\phi}(t) \exp\{-i\boldsymbol{\kappa}(t) \cdot \mathbf{x}\}, \quad (\text{A.1})$$

where $\boldsymbol{\kappa}(t)$ is the time-dependent wave-number vector. By eliminating the pressure from the linearized momentum equation through the solution of the Poisson equation, the resulting set of equations for the Fourier coefficients can be written as:

$$d_t \hat{u}_i = \hat{u}_1 \alpha \left(\frac{2\boldsymbol{\kappa}_i \boldsymbol{\kappa}_1}{\boldsymbol{\kappa}^2} - \delta_{ii} \right), \quad (\text{A.2a})$$

$$d_t \hat{Y} = -\hat{u}_1 \beta_s \xi, \quad (\text{A.2b})$$

$$d_t \hat{T} = -(\gamma - 1) \alpha \hat{T}, \quad (\text{A.2c})$$

$$d_t \boldsymbol{\kappa}_i = -\boldsymbol{\kappa}_1 \alpha \delta_{ii}. \quad (\text{A.2d})$$

The analytical solution of this set of differential equations can be written in the following form:

$$\hat{u}_1(t) = \hat{u}_{1,s} \xi \frac{\boldsymbol{\kappa}^2}{\boldsymbol{\kappa}^2}, \quad (\text{A.3a})$$

$$\hat{u}_\alpha(t) = \hat{u}_{1,s} \frac{\boldsymbol{\kappa}_\alpha}{\boldsymbol{\kappa}_1} \left(\frac{\boldsymbol{\kappa}^2}{\boldsymbol{\kappa}^2} - 1 \right) + \hat{u}_{\alpha,s} \quad \text{for } \alpha = \{2, 3\}, \quad (\text{A.3b})$$

$$\hat{Y}(t) = -\hat{u}_{1,s} \beta_s J + \hat{Y}_s \quad \text{with } J = \int_{-t_c}^0 \xi^2 \frac{\boldsymbol{\kappa}^2}{\boldsymbol{\kappa}^2} dt', \quad (\text{A.3c})$$

$$\hat{T}(t) = \hat{T}_s \xi^{\gamma-1}, \quad (\text{A.3d})$$

where $\boldsymbol{\kappa} = (\boldsymbol{\kappa}_1 \xi, \boldsymbol{\kappa}_2, \boldsymbol{\kappa}_3)^T$, and $\boldsymbol{\kappa}$ is the initial wave number vector at the beginning of the compression phase, $t = -t_c$. Finally, expressions describing the temporal evolution of the normal stresses and variances of species mass fractions and temperature can be obtained by multiplying Eqs. (A.3) by its complex conjugate, substituting the isotropic energy and scalar spectra, and integrating in spherical coordinates over all wave numbers. This results in the integral expressions that are given by Eqs. (12), which can be solved numerically for prescribed values of \mathcal{T}_u , \mathcal{T}_Y , \mathcal{T}_T , β_s , and ξ .

References

- [1] International Energy Outlook. Report No. DOE/EIA-0484(2009); 2009 <<http://www.eia.doe.gov/oiaf/ieo/index.html>>.
- [2] K.H. Casleton, R.W. Breault, G.A. Richards, Combust. Sci. Technol. 180 (2008) 1013–1052.
- [3] M. Chaos, F.L. Dryer, Combust. Sci. Technol. 180 (2008) 1053–1096.
- [4] C.-J. Sung, C.K. Law, Combust. Sci. Technol. 180 (2008) 1097–1116.
- [5] S.M. Walton, X. He, B.T. Zigler, M.S. Wooldridge, Proc. Combust. Inst. 31 (2007) 3147–3154.
- [6] E.L. Petersen, D.M. Kalitan, A.B. Barrett, S.C. Reehal, J.D. Mertens, D.J. Beerer, R.L. Hack, V.G. McDonell, Combust. Flame 149 (2007) 244–247.
- [7] D.F. Davidson, R.K. Hanson, Shock Waves 19 (2009) 271–283.
- [8] M. Chaos, F.L. Dryer, Int. J. Chem. Kinet. 42 (2010) 143–150.
- [9] J.F. Griffiths, Q. Jiao, W. Kordylewski, M. Schreiber, J. Meyer, K.F. Knoche, Combust. Flame 93 (1993) 303–315.
- [10] D. Lee, S. Hochgreb, Combust. Flame 114 (1998) 531–545.
- [11] J. Würmel, J.M. Simmie, Combust. Flame 141 (2005) 417–430.
- [12] G. Mittal, C.-J. Sung, Combust. Flame 145 (2006) 160–180.
- [13] C. Strozzi, J. Sotton, A. Mura, M. Bellenoue, Meas. Sci. Technol. 20 (2009) 125403.
- [14] P. Guibert, A. Keromnes, G. Legros, Flow, Turb. Combust. 84 (1) (2010) 79–95.
- [15] J.E. Elsworth, W.W. Haskell, I.A. Read, Combust. Flame 13 (1969) 437–438.
- [16] D.R. Lancaster, Effects of engine variables on turbulence in a spark-ignition engine, SAE Paper 760159; 1976. p. 671–88.
- [17] R.J. Tabaczynski, D.P. Hoult, J.C. Keck, J. Fluid Mech. 42 (1970) 249–255.
- [18] J.C.R. Hunt, D.J. Carruthers, J. Fluid Mech. 212 (1990) 497–532.
- [19] C. Cambon, J.F. Scott, Ann. Rev. Fluid Mech. 31 (1999) 1–53.
- [20] I. Hadžić, K. Hanjalić, Phys. Fluids 13 (6) (2001) 1739–1747.
- [21] M.T. Donovan, X. He, B.T. Zigler, T.R. Palmer, M.S. Wooldridge, A. Atreya, Combust. Flame 137 (2004) 351–365.
- [22] T. Poinsot, D. Veynante, Theoretical and Numerical Combustion, R.T. Edwards, Inc., Philadelphia, PA, 2001.
- [23] P.A. Durbin, B.A. Petterson Reif, Statistical Theory and Modeling for Turbulent Flows, John Wiley & Sons, Inc., 2001.
- [24] J.C.R. Hunt, Fluid Dyn. Trans. 9 (1977) 121–152.
- [25] A.M. Savill, Ann. Rev. Fluid Mech. 19 (1987) 531–575.
- [26] S.B. Pope, Turbulent Flows, Cambridge University Press, Cambridge, 2000.
- [27] R.O. Fox, Computational Models for Turbulent Reacting Flows, Cambridge University Press, Cambridge, 2003.

- [28] N. Peters, *Turbulent Combustion*, Cambridge University Press, Cambridge, 2000.
- [29] S. Tanaka, F. Ayala, J.C. Keck, *Combust. Flame* 133 (2003) 467–481.
- [30] R.J. Kee, J.F. Grcar, M.D. Smooke, J.A. Miller, E. Meeks. PREMIX: A FORTRAN program for modeling steady laminar one-dimensional premixed flames of turbulent combustion. Sand85-8240, Sandia National Laboratories, Livermore, 1983.
- [31] J. Li, Z. Zhao, A. Kazakov, M. Chaos, F.L. Dryer, J.J. Scire Jr., *Int. J. Chem. Kinet.* 39 (2007) 109–136.
- [32] R.A. Fraser, R.A. Bracco, Cycle-resolved LDV integral length scale measurements investigating clearance height scaling, isotropy, and homogeneity in an I.C. engine. SAE Paper 890615, 1989.
- [33] M.S. Wooldridge, D. Karwat, Private communication, 2010.
- [34] W.T. Peschke, L.J. Spadaccini, Determination of autoignition and flame speed characteristics of coal gases having medium heating value. Report No. EPRI-AP-4291, United Technologies Research Center, 1985.
- [35] J.E. Dec, *Proc. Combust. Inst.* 32 (2009) 2727–2742.
- [36] Y.B. Zeldovich, *Combust. Flame* 39 (1980) 211–214.
- [37] J.H. Chen, E.R. Hawkes, R. Sankaran, S.D. Mason, H.G. Im, *Combust. Flame* 145 (2006) 128–144.
- [38] F.L. Dryer, M. Chaos, *Combust. Flame* 152 (2008) 293.
- [39] G. Mittal, M.P. Raju, C.-J. Sung, *Combust. Flame* 155 (2008) 417–428.